Defense Threat Reduction Agency
8725 John J. Kingman Road, MS
6201 Fort Belvoir, VA 22060-6201

DTRA-TR-21-18

TECHNICAL REPORT

Exploration of Damage Mechanisms in MEMS based Memory and Logic Devices

Distribution Statement A. Approved for public release; distribution is unlimited.
This report is UNCLASSIFIED.

March 2021

HDTRA1-15-1-0027

Prepared by: Bruce Alphenaar

University of Louisville,Louisville, KY 40292

REPORT DOCUMENTATION PAGE

Form Approved
OMB No. 0704-0188

The public reporting burden for this collection of information is estimated to average 1 hour per response, including the time for reviewing instructions, searching existing data sources, gathering and maintaining the data needed, and completing and reviewing the collection of information. Send comments regarding this burden estimate or any other aspect of this collection of information, including suggestions for reducing the burden, to Department of Defense, Washington Headquarters Services, Directorate for Information Operations and Reports (0704-0188), 1215 Jefferson Davis Highway, Suite 1204, Arlington, VA 22202-4302. Respondents should be aware that notwithstanding any other provision of law, no person shall be subject to any penalty for failing to comply with a collection of information if it does not display a currently valid OMB control number.
PLEASE DO NOT RETURN YOUR FORM TO THE ABOVE ADDRESS.

1. REPORT DATE *(DD-MM-YYYY)*
20-02-2021

2. REPORT TYPE
Final

3. DATES COVERED *(From - To)*
01-07-2015 - 30-06-2020

4. TITLE AND SUBTITLE
Exploration of Damage Mechanisms in MEMS based Memory and Logic Devices

5a. CONTRACT NUMBER

5b. GRANT NUMBER
HDTRA1-15-1-0027

5c. PROGRAM ELEMENT NUMBER

6. AUTHOR(S)
Alphenaar, Bruce; McNamara, Shamus; Walsh, Kevin; Alles, Michael; Arutt, Charles; Shuvra, Pranoy; Liao, Wenjun; Gong, Huiqi; Davidson, Jim

5d. PROJECT NUMBER

5e. TASK NUMBER

5f. WORK UNIT NUMBER

7. PERFORMING ORGANIZATION NAME(S) AND ADDRESS(ES)
University of Louisville, Louisville, KY 40292
Vanderbilt University, Nashville, TN

8. PERFORMING ORGANIZATION REPORT NUMBER

9. SPONSORING/MONITORING AGENCY NAME(S) AND ADDRESS(ES)
Defense Threat Reduction Agency
8725 John J. Kingman Road
Fort Belvoir, VA 22060-6201

10. SPONSOR/MONITOR'S ACRONYM(S)
DTRA

11. SPONSOR/MONITOR'S REPORT NUMBER(S)
DTRA TR-21-18

12. DISTRIBUTION/AVAILABILITY STATEMENT
Unclassified, for general distribution

13. SUPPLEMENTARY NOTES

14. ABSTRACT
The goal of this project was to explore the influence of radiation on critical structures of MEMS sensors, memory and logic devices; to reveal the extent to which radiation influences the MEMS properties; and to determine the mechanisms behind the radiation induced changes. To this end, silicon MEMS resonators were designed and fabricated and exposed to X-ray and proton irradiation, and the mechanisms behind the observed changes were determined.

15. SUBJECT TERMS

16. SECURITY CLASSIFICATION OF: a. REPORT	b. ABSTRACT	c. THIS PAGE	17. LIMITATION OF ABSTRACT	18. NUMBER OF PAGES	19a. NAME OF RESPONSIBLE PERSON
U	U	U	SAR	25	Bruce Alphenaar
					19b. TELEPHONE NUMBER *(Include area code)* 502-727-9493

Standard Form 298 (Rev. 8/98)
Prescribed by ANSI Std. Z39.18

Final Report HDTRA1-15-1-0027
EXPLORATION OF DAMAGE MECHANISMS IN MEMS BASED MEMORY AND LOGIC DEVICES

Abstract

The beneficial size, weight, and power requirements provided by micro-electromechanical (MEMS) and nanoelectromechanical (NEMS) memory, logic and sensors for military systems operating in extreme radiation environments make it essential that the effects of radiation on MEMS/NEMS devices be investigated. Here, we explore the influence of radiation on critical structures of MEMS memory and logic devices to reveal the extent to which radiation influences the MEMS properties and to determine the mechanisms behind the radiation induced changes. Radiation induced modifications to electrical and mechanical performance is probed via the frequency response of MEMS/NEMS cantilevers having micron to submicron dimensions and containing a variety of materials. MEMS/NEMS structures that display a non-linear response to deflecting forces provide an ultra-sensitive probe to both long term and in-situ radiation effects. In this way we uncover radiation damage mechanisms whose fundamental understanding is essential for future MEMS/NEMS applications.

I) Introduction

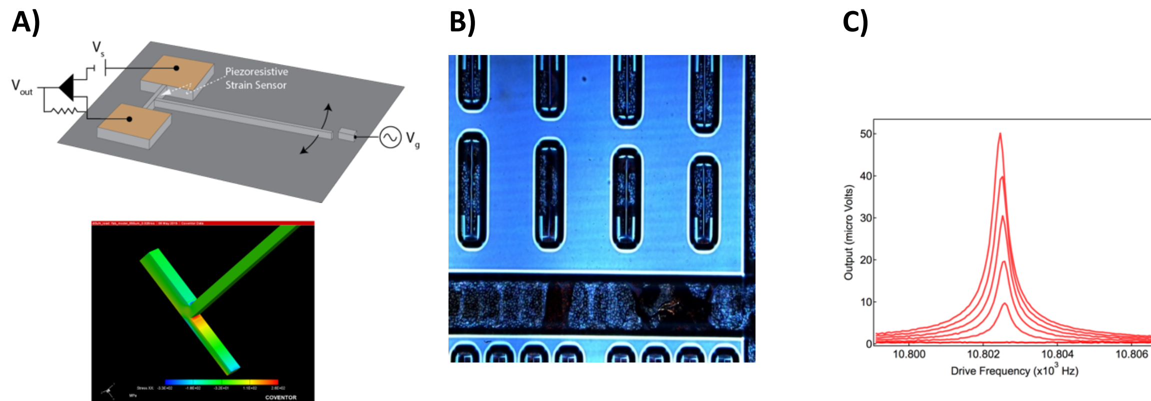

Figure 1. Design, simulation and testing of preliminary MEMS structure **A)** Horizontal cantilever driven by ac gate voltage results in strain profile on base that produces piezoresistive change in base resistance **B)** Multiple cantilevers on SOI wafer prior to dicing **C)** Cantilever output versus driving frequency for different sense biases.

Much of the existing work studying the influence of radiation on MEMS consists of tests on commercially available MEMS devices with radiation levels similar to those existing in space applications. Micromechanical memory, logic, and sensing devices rely on the bi-stable deflection of micro-scale mechanical resonators or diaphragms for operation. Such devices can be sensitive to part-per-million changes in Young's modulus but experiments able to detect such small changes have not been done. Given the lack of available systematic studies, an understanding of the fundamental physics of radiation effects in MEMS memory and logic elements requires a step-by-step approach, consisting of the following elements:

(1) Fundamental Model Systems and Calculations: Microscale resonators (as shown in Fig. 1 above) and diaphragms are simple enough that the influence of radiation can be determined independent of extraneous complications (e.g. material interactions, built-in potentials, dielectric charging, and measurement electronics). Nevertheless, their operating principle is essential to almost all MEMS memory and logic components.

(2) Exposure Source, Time and Energy Dependencies: Exposure to radiation sources that can either induce trapped charge effects only (e.g., x-rays or gamma rays) or trapped charge and displacement damage effects (e.g., protons) will assist in determining the failure mechanisms. Radiation exposure has an immediate impact on MEMS device function. In-situ monitoring of MEMS operation during exposure is essential for predicting function during WMD attack, or nuclear catastrophe, particularly for memory storage and logic devices. Time and temperature healing experiments will determine the energy distribution of trapped charge.

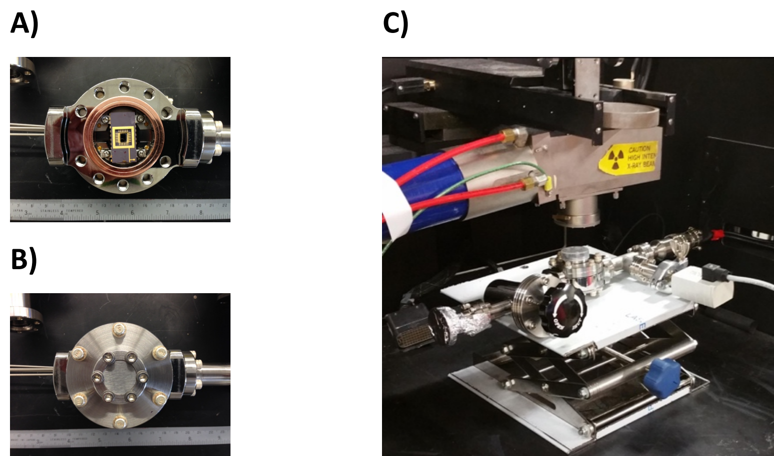

Figure 2. Vacuum chamber used to test MEMS devices during X-ray exposure **A)** Open chamber containing MEMS device **B)** Chamber sealed with Be window **C)** Chamber as used in X-ray exposure tests.

(3) *Bi-stable Memory and Logic Elements* The knowledge gained in previous sections provides the basis for a study of memory and logic elements relying on bi-stable mechanical structures. These are particularly sensitive to radiation induced changes in their switching voltage and transition to chaotic motion. The non-linear forces allow for a more sensitive determination of structural changes than is possible using a simple resonator.

(4) *Device Geometry and Materials Dependencies:* As the dimensions of the resonators are reduced—transitioning from *micro* to *nano* electromechanical systems—new damage mechanisms and increased sensitivity to existing mechanisms arise. Resonators coated with a variety of dielectrics, disordered semiconductors, piezoelectrics, and ferromagnetics are used to determine the influence of radiation on under-characterized material systems of interest for MEMS application

II) Total-Ionizing-Dose Effects in Piezoresistive Micromachined Cantilever

In this section, the radiation response of a T-shaped, asymmetric silicon piezoresistive micromachined cantilever fabricated from an SOI starting wafer is evaluated. The devices are

irradiated up to a total dose of 2.1 Mrad(SiO_2) with 10-keV X-rays. The resonance frequency decreases as the total dose increases, with a change of about 25 ppm at the maximum dose. A physical explanation is proposed, based on radiation-induced acceptor depassivation and changes in the elastic modulus due to carrier concentration changes. Finite element simulations show that a decreasing Young's modulus in the surface region due to radiation-induced increase in carrier density is consistent with the measured decrease in resonance frequency.

The device structure is shown in Fig. 3. The cantilever is fabricated from an SOI starting wafer. The fabrication process starts with a (100) p-type (boron doped) SOI wafer. The doping concentrations of the device and substrate layers are the same, around 2×10^{18} cm^{-3}. The resistivity of both silicon layers is 0.036 Ω-cm. The dimensions of the devices are shown in Fig. 3d and Table 1.

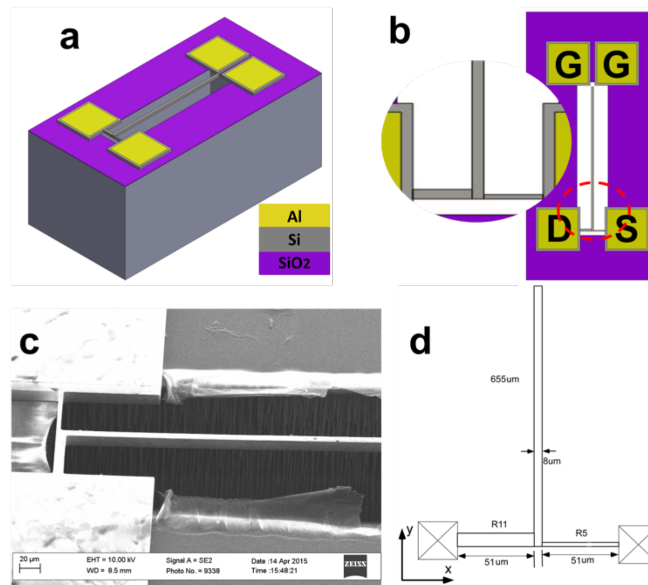

Figure 3. Device structure: (a) 3-D overview of the asymmetric cantilever, (b) top view of the cantilever; the inset shows the asymmetric beam anchors, (c) SEM image of the cantilever, (d) device dimensions.

TABLE I DEVICE LAYER DIMENSIONS

Layer	Thickness (μm)
Electrode (Al)	0.618
Device (Si)	15
Oxide (SiO_2)	1.5
Substrate (Si)	500
Electrode (Al)	0.618

In order to actuate the cantilever, an AC voltage is applied to the two electrodes near the free end, as shown in Fig. 3b (gate electrodes), and constant DC voltage is applied to the anchor electrodes (drain and source electrodes). An electric field forms between the free end of the cantilever and the gate electrode, which leads to an external force on the free end of the cantilever. The external force results in displacement of the free end. Since the gate is actuated by an AC signal, the base anchor beam can oscillate. The amount of bending depends on the displacement of the free end. The bending imposes compressive and tensile stress in different regions of the anchor. This changes the overall resistance. This

resistance change can be calculated by measuring the current change in the beam anchor. For an asymmetric cantilever, the widths of the anchors are different, as shown in the insets of Figs. 3b and Fig. 3d. For a DC voltage, the wider base region (R11 with width of 11 μm) is displaced less than the narrower base region (R5 with width of 5 μm), due to higher stiffness. This structure leads to larger net resistance change, and thus much higher sensitivity (15 to 200 times), compared with symmetric designs. The largest change is obtained at the resonance frequency.

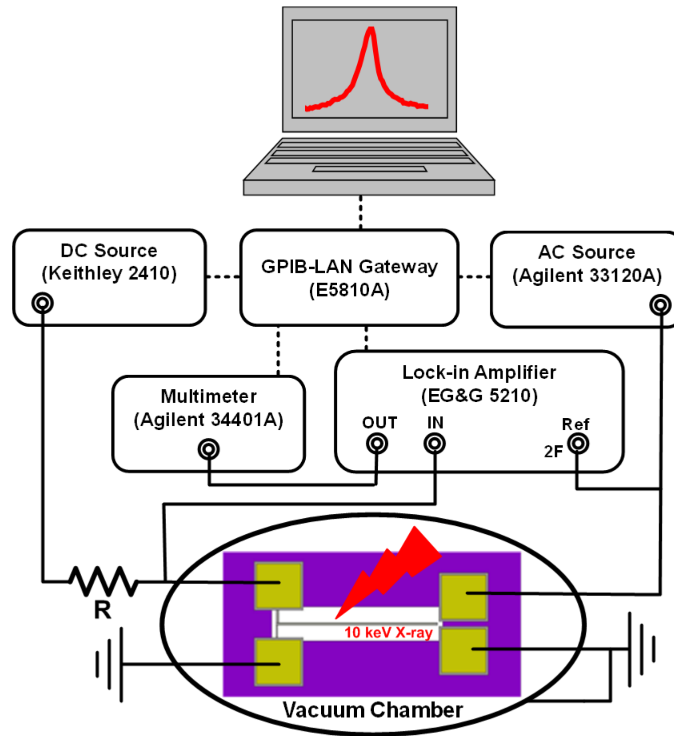

Figure 4. Electrical measurement setup for MEMS cantilever.

Fig. 4 shows the electrical measurement setup. A Keithley 2410 source meter is used as the DC source. Real time current data are recorded during the measurement. An Agilent 33120 provides the driving AC signal, with a frequency of approximately 10 kHz. A constant DC voltage of 50 mV is applied to the beam anchor. The resistance change due to the oscillation of the cantilever results in a current change in the beam anchor. There is a 265 Ω series resistor (about the same magnitude as the resistance of the beam anchor) in the circuit. The current change results in a voltage change across the series resistor. This voltage drop serves as the input signal for a lock-in amplifier. The lock-in amplifier uses a 2F external reference signal from the driving AC source, because the device resonates at two times the driving frequency. A vacuum chamber compatible with the 10-keV X-ray source is set up in the test system. The vacuum chamber has a thin beryllium window, which has a very low X-ray absorption coefficient. The system allows measurement of pressure, temperature, and device response during radiation. Because cantilever devices can be quite sensitive to temperature and pressure, all experiments were done under constant temperature (~295 K) and pressure (2×10^{-6} mbar). Small changes in temperature and pressure typical of the kinds of variations observed during an irradiation sequence were found to produce shifts in device characteristics that were significantly less than the radiation-induced changes reported below. The responses of more than 10 cantilever structures were evaluated; representative results are shown

In situ measurements with DC and AC voltages applied are taken so that the device under test operates

in dynamic mode during irradiation. Devices are irradiated with 10-keV X-rays at a dose rate of 31.5 krad(SiO_2)/min. The pre-irradiation results are very stable, as shown in Fig. 5(a). Figs. 5(b) and (c) show that the resonance frequency decreases as the total dose increases, with a maximum decrease of approximately 0.56 Hz (25.48 ppm change).

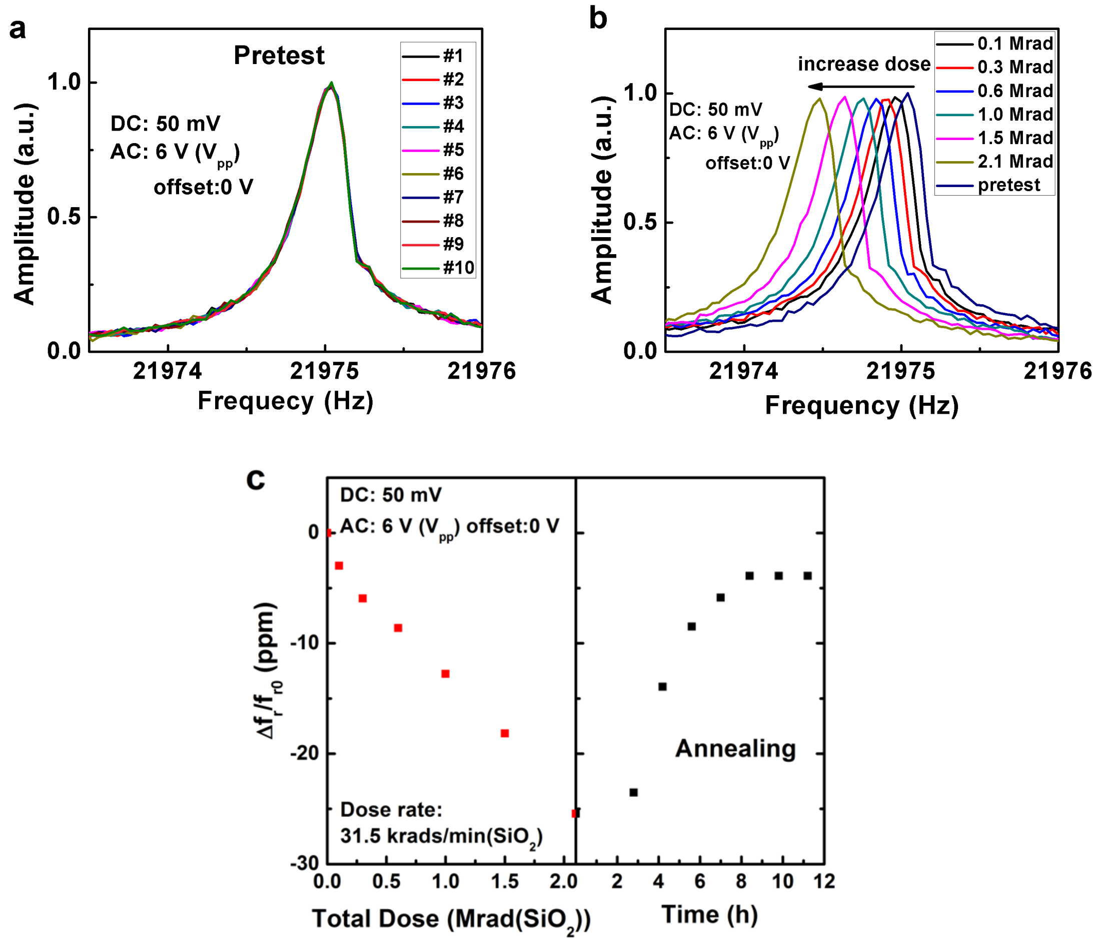

Figure 5. Frequency response near the resonance peak (a) before irradiation and (b) as a function of X-ray irradiation. Also shown (c) are the position of the resonance peak as a function of dose and as a function of post-irradiation annealing.

During post-irradiation annealing, the resonance frequency recovers to nearly the initial value within a few hours, as shown in Fig. 3(c). The shift in resonance frequency does not depend significantly on the polarity or magnitude of the applied DC bias over the range of typical biases investigated; approximately the same magnitude of resonance frequency shift is observed for 50 mV, -50 mV, and 0 V biases.

We have considered a number of physical processes that may affect the observed changes in resonance frequency. Calculations indicate that the size and spacing of this MEMS device make it unlikely that Coulomb forces from radiation-induced surfaces charges alone can lead to the observed changes in resonance frequency. But a contributing role for surface charge cannot be excluded. Changes in mass are also known to affect the resonance frequency of similar devices [5]. So adsorbed gases were also considered. However, controlled exposures of these devices to residual gases at expected levels showed

no effect on the resonance frequency, with or without radiation.

The most plausible candidate for the dominant factor that accounts for the observed changes in resonance frequency of these devices with radiation exposure appears to be a change in Young's modulus caused by a change in radiation-induced carrier density. According to simple beam theory, the nth mode resonance frequency, f_n, of a cantilever is

$$f_n = \frac{\beta_n^{\ 2}}{2\pi L^2}\sqrt{\frac{YI}{\rho A}}$$

where *Y* is Young's modulus, *I* is the cross-sectional moment of inertia, L is the length of the cantilever, ρ is the beam mass density, and *A* is the beam cross-section area. β_n is the Eigen value from the equation: $\cos\beta_n \cosh\beta_n + 1 = 0$; $\beta_0 = 1.875$, $\beta_1 = 4.694$, and $\beta_2 = 7.855$ correspond to the first three resonance modes for a singly attached cantilever. The resonance mode we measured is the first resonance mode. Using the actual device dimensions (values taken directly from the calibrated SEM image) in the equation, $f_1 = 20795.5$ Hz. All devices tested had an observed resonance of ~ 20 kHz, which is consistent with this estimate.

Elasticity is the relationship between stress σ and strain ε, which is expressed by Hooke's law: $\sigma = C\varepsilon$, where *C* is the stiffness. For isotropic materials, *C* can be represented by a constant value of Young's modulus, *Y*. For anisotropic materials, a fourth rank tensor with 81 terms represents the stiffness. Considering the cubic symmetry of silicon, the tensor is represented by a 6×6 matrix, and Hooke's law can be rewritten as:

$$\begin{bmatrix} \sigma_1 \\ \sigma_2 \\ \sigma_3 \\ \sigma_4 \\ \sigma_5 \\ \sigma_6 \end{bmatrix} = \begin{bmatrix} c_{11} & c_{12} & c_{12} & 0 & 0 & 0 \\ c_{12} & c_{11} & c_{12} & 0 & 0 & 0 \\ c_{12} & c_{12} & c_{11} & 0 & 0 & 0 \\ 0 & 0 & 0 & c_{44} & 0 & 0 \\ 0 & 0 & 0 & 0 & c_{44} & 0 \\ 0 & 0 & 0 & 0 & 0 & c_{44} \end{bmatrix} \begin{bmatrix} \varepsilon_1 \\ \varepsilon_2 \\ \varepsilon_3 \\ \varepsilon_4 \\ \varepsilon_5 \\ \varepsilon_6 \end{bmatrix}$$

The cantilever orientation is shown in Fig. 6. The electrostatic force is applied along the [110] direction and the cantilever bends in the [110] direction. The elastic modulus that affects the resonance frequency is described by:

$$Y_{110} = \frac{4(c_{11} - c_{12})(c_{11} + 2c_{12})c_{44}}{2c_{11}c_{44} + (c_{11} - c_{12})(c_{11} + 2c_{12})}$$

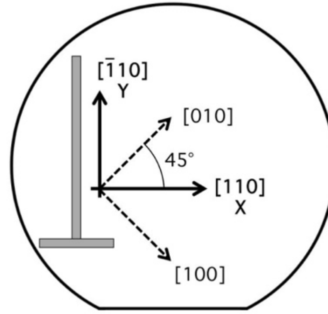

Figure 6. Cantilever orientation with respect to wafer orientations. The beam bends at the [110] direction.

We now discuss how carrier concentration changes during X-ray irradiation. Complexes of hydrogen with dopants in silicon have been extensively studied both experimentally and theoretically. In boron-doped silicon, interstitial hydrogen rests between boron and neighboring silicon atoms. When the hydrogen is released into the silicon crystal, the charge state depends on the Fermi level. In p-type silicon, the most stable interstitial hydrogen state is H^+.

Ionizing radiation results in electron-hole pair generation. Experimental results shows that the activation energy for B-H dissociation is (1.28±0.03) eV. When the cantilever is irradiated, acceptor depassivation is facilitated during the hole transport process in Si, since the presence of minority carriers reduces the bonding energy of B-H from 0.61 eV to 0.45 eV. We represent this process schematically as:

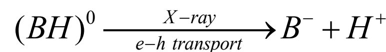

$$(BH)^0 \xrightarrow[e-h\ transport]{X-ray} B^- + H^+$$

This hydrogen release process is more significant near the interface. The depassivation of acceptors leads to an increase in carrier (hole) concentration at the surface of the beam. During annealing (following termination of irradiation), some of the acceptors are passivated again, via the reverse process, leading to a decrease in carrier concentration:

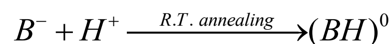

$$B^- + H^+ \xrightarrow{R.T.\ annealing} (BH)^0$$

We now consider how an increase in carrier concentration in the cantilever beam (shown schematically in Fig. 7a) due to acceptor depassivation can cause Young's modulus and the resonance frequency to decrease during irradiation, and then increase during annealing as some dopants are repassivated, and the carrier concentration decreases. To support this analysis, COMSOL simulations were performed. In these simulations, the material coordinate is aligned with the [100] direction (dotted axes in Fig. 7), while the device anchor is aligned with the [110] direction (solid axes in Fig. 7).

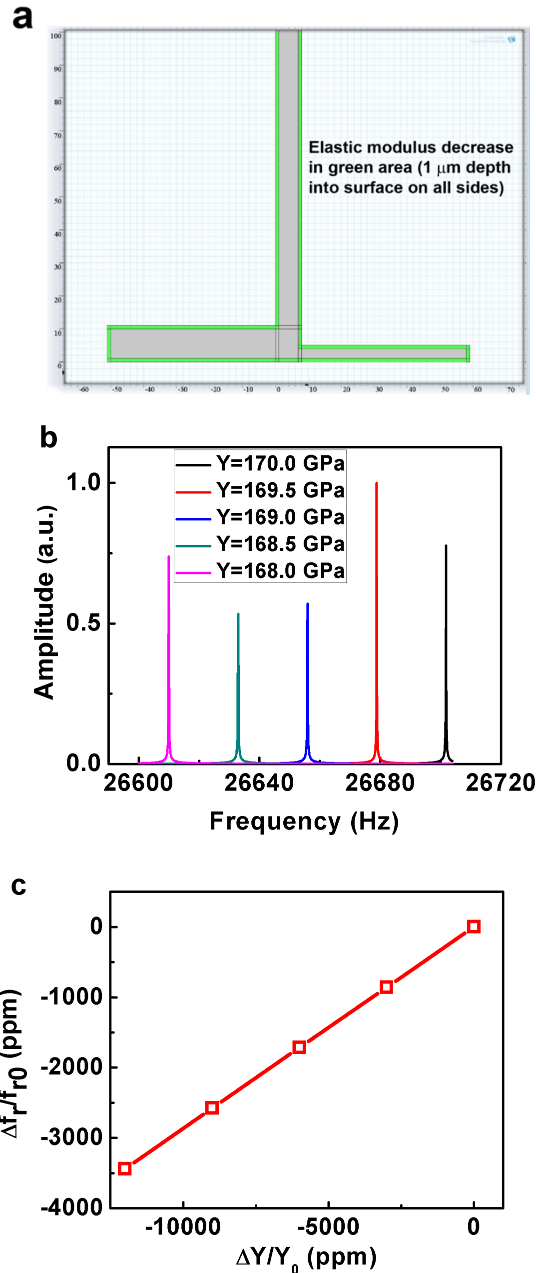

Figure 7. (a) Cross section of cantilever for COMSOL simulation. Assume Young's modulus of surface area (green region, 1 μm depth into surface on all sides) changes, (b) resonance peaks for different Young's modulus in green region, (c) resonance frequency change as function of Young's modulus change in the surface area.

Young's modulus for intrinsic silicon along the [110] direction is 169 GPa. We simulated an elastic modulus change from 170 GPa to 168 GPa in a 1 μm depth at the surface on all sides of the cantilever, shown as the green region in Fig. 7a. The elastic modulus in the deep bulk region is assumed to remain constant during irradiation and annealing. The density of silicon is 2.33 g/cm^3, and Poisson's ratio is 0.28. Device dimensions are those shown in Fig. 3d. The simulation results are shown in Figs. 7b and Fig. 7c. The resonance frequency decreases linearly as Young's modulus in the surface area decreases, as shown in Fig. 7c:

$$\frac{\Delta f_r}{f_{r0}} = 0.29\frac{\Delta Y}{Y_0}$$

These simulations suggest that a 25 ppm change of resonance frequency corresponds to a ~ 86 ppm change in Young's modulus. We now consider whether such a change in Young's modulus is plausible in irradiated Si beams.

Keyes demonstrated in 1961 that dopant atoms cause a decrease in the shear elastic modulus c_{44} in semiconductors. For p-type silicon, using the theory of Keyes, we may estimate this change:

$$\Delta c_{44} = -\frac{1}{5}(\frac{8\pi}{3})^{\frac{2}{3}}\frac{d^2}{h^2}(m_{v1}{}^{*}p_1^{\frac{1}{3}} + m_{v2}{}^{*}p_2^{\frac{1}{3}})$$

where Δc_{44} is the change in modulus with respect to the value of intrinsic silicon, *d* is the deformation potential (15.4 eV), *h* is Planck's constant, $m_{v1}{}^{*}$ is the light hole effective mass, $m_{v2}{}^{*}$ is the heavy hole effective mass, p_1 is the concentration of light holes, and p_2 is concentration of heavy holes. The resistivity of the silicon wafer in this work is 0.036 Ω-cm. Hence, the initial hole concentration is $\sim 1.13\times 10^{18}\,\mathrm{cm}^{-3}$. From Eqs. (2) and (3), we find:

$$Y_{110} = 168.3\ GPa$$

Recall that, after irradiation, COMSOL simulations suggest that a change in Young's modulus of 86 ppm will produce a resonance frequency shift similar to the one observed in experiments. From Eqs. (2) and (3), we find that the correspondence change in carrier concentration near surface is:

$$\Delta p/p = 6.5\%$$

That such a change in dopant density is plausible with 2 Mrad(SiO_2) X-ray irradiation is suggested by work performed by Witczak et al., who demonstrated up to a 20% change in density of activated dopants in studies of MOS capacitors irradiated to 50 krad(SiO_2). The amount of dopant activation or passivation in a particular device will of course depend on device structure and processing, so additional work is required to understand the nature of these processes in MEMS structures in more detail.

We also note that the above analysis may overestimate the actual change in the carrier concentration because it considers only the change in Young's modulus in the surface region and only the change in c_{44}. If instead we assume the entire silicon layer changes uniformly, from equation (1), we find:

$$\frac{\Delta f_r}{f_{r0}} = (1+\frac{\Delta Y}{Y_0})^{\frac{1}{2}} - 1$$

Using Taylor expansion, and discarding the higher order terms:

$$\frac{\Delta f_r}{f_{r0}} = 0.5\frac{\Delta Y}{Y_0}$$

Thus a 25 ppm change in resonance frequency would require only a 50 ppm change in Young's modulus for the case of uniform dopant depassivation. Further, experimental data show that c_{11}, c_{12} and c_{44} all decrease for doped silicon [27], which further reduces the amount of dopant passivation required to produce the observed response, reinforcing the plausibility of the proposed mechanism.

III) Proton-Induced Total-Ionizing-Dose and NIEL Effects on Silicon Based MEMS Resonators

Next, the proton radiation response is evaluated for the piezoresistive micro-machined silicon resonator. The devices were irradiated with a proton beam at energies of 2 MeV and 0.8 MeV. Small, but significant, changes in the resonant frequency of the test devices at mechanical response levels that matter for space applications are observed during irradiation. Both ionization and nonionizing energy loss (NIEL) affect the resonant frequency. Ionization effects cause the resonant frequency to decrease during irradiation; it recovers at room temperature after ~ 10 h of annealing. A model based on radiation-induced acceptor depassivation and changes in the elastic modulus due to carrier concentration change may explain these results. NIEL causes carrier removal, which causes an increase in Young's modulus and a corresponding increase in the resonant frequency. The competing effects between ionization and NIEL are reported for protons at different energies. For higher energy protons, ionization effects dominate, while NIEL effects dominate for lower energy protons. SRIM simulations are used to explain these competing effects.

The resonator, which is fabricated on a p-type SOI wafer, is shown in detail in Fig. 3. The experimental setup for the resonators is the same as described above in Fig. 4. The behavior of devices in pre-irradiation tests is very stable, as shown in Fig. 8a. During 2 MeV proton irradiation, the resonant frequency (frequency at which the amplitude is maximum) decreases with fluence, as shown in Fig. 8b. For 0.8 MeV proton irradiation, the resonant frequency increases with fluence, as shown in Fig. 8c, consistent with previous results. Based on separate measurements and calculations of the temperature sensitivity, differences in chip heating due to the difference in flux between the two exposures may account for at most 10 ppm (~1 ℃) of this difference; the remainder is attributed primarily to different ratios and effects of NIEL and ionization in the two cases.

The relative changes in the resonant frequency as a function of fluence and as a function of annealing time are shown in Fig. 9. During post-irradiation annealing, the resonant frequency increases for both proton energies. The beam anchor (as shown in Fig. 3b) resistance of the resonators is monitored with a HP4156B semiconductor parameter analyzer during proton irradiation. In both cases, the resistance increases with proton fluence, with little recovery during post-irradiation room-temperature annealing, as shown in Figs. 9a and 9b.

Previous work on X-ray irradiation of silicon oscillators shows that ionization effects cause resonant frequency decreases during irradiation that recover in about 10 h during post-irradiation room temperature annealing, while the recovery of NIEL effects may take days. The resonant frequency increase during annealing is attributed to the recovery of the ionization portion of the radiation-induced change. The contributions of ionization and NIEL can be extracted separately from the overall change, as shown in Fig. 10.

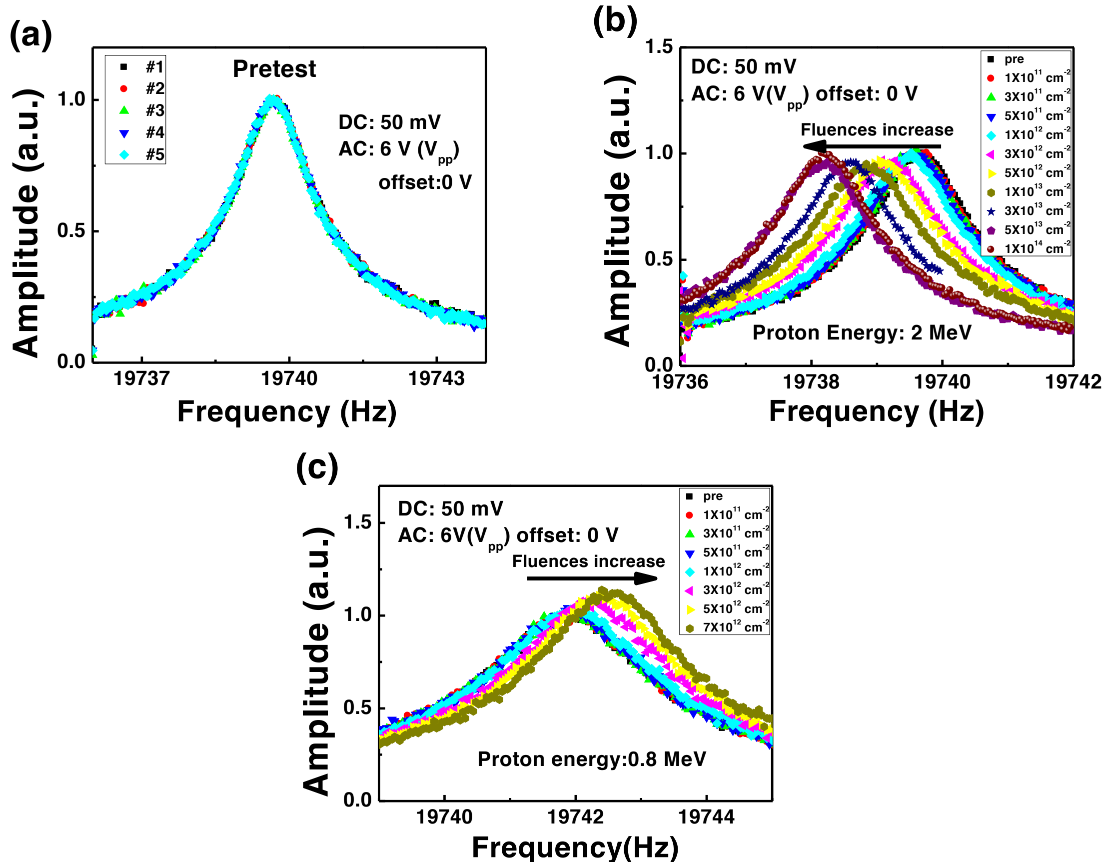

Figure 8. Frequency response near the resonant peak (a) before irradiation, and as a function of fluence for (b) 2 MeV protons and (c) 0.8 MeV proton irradiation.

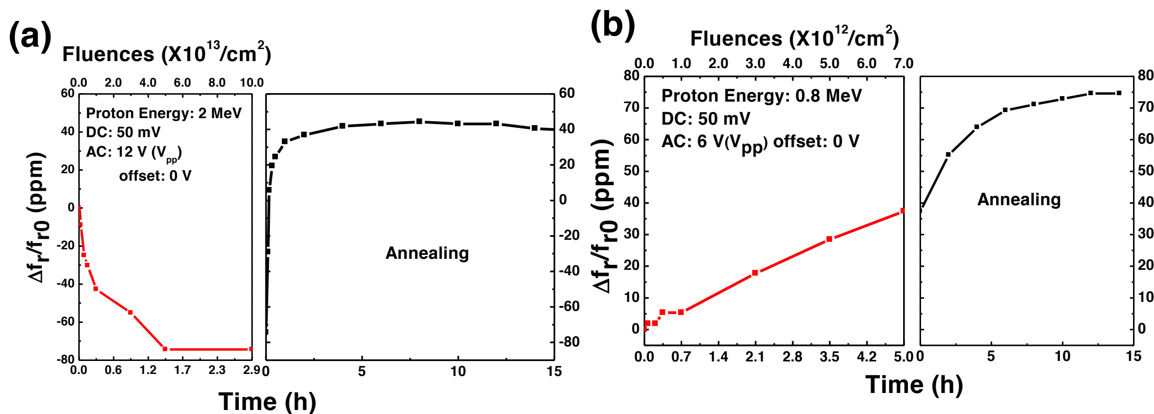

Figure 9. The relative changes in the resonant frequency as a function of fluence and as a function of post-irradiation annealing for (a) 2 MeV protons and (b) 0.8 MeV proton.

The extracted ionization portion of the change is shown in Fig. 11a. The amount of change produced by ionization for the 2-MeV proton irradiation is similar to previous X-ray results, while the 0.8 MeV protons produce less ionization-induced change. This is because the flux of 0.8 MeV protons is about 24 times

lower than the flux of 2 MeV protons. Thus, it takes 4.25 h to reach an ionization dose of 6 Mrad(SiO_2) for 0.8 MeV protons, and only minutes for 2 MeV protons. Because of annealing effects during the exposure, the effective ionization-induced change for 0.8 MeV protons is much smaller than the change for 2 MeV protons. The recovery times shown in Figs. 9a and 9b are both on the order of 10 h, which is consistent with previous X-ray results. The extracted NIEL-induced resonant frequency change is shown in Fig. 11b. 0.8 MeV proton irradiation produces more change compared with 2 MeV protons. Fig. 11c shows the anchor resistance change during proton irradiation, which is produced by carrier removal effects.

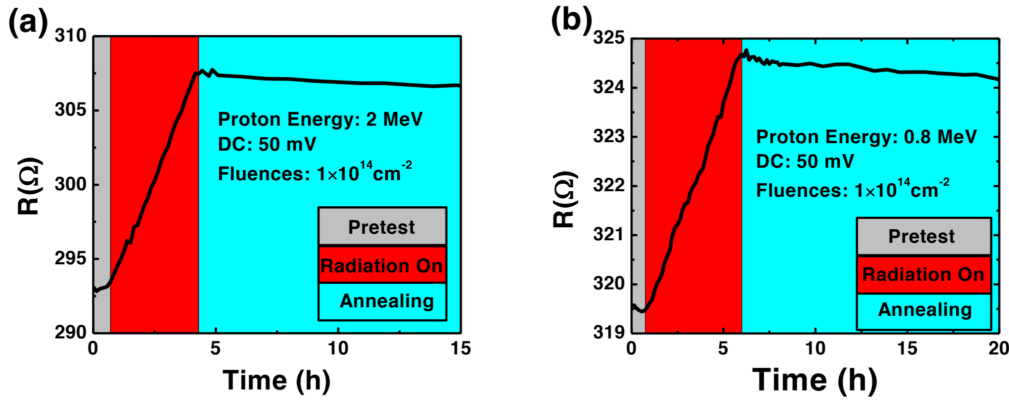

Figure 10. The anchor resistance response is also shown for (a) 2 MeV protons and (b) 0.8 MeV protons.

High energy proton irradiation produces defect complexes in silicon that will reduce the carrier concentration due to carrier removal. Defect complexes act as trapping centers in silicon. If the trapping centers are below the Fermi level in n-type material or above the Fermi level in p-type material, they will be able to trap majority carriers. For heavily doped *p*-type silicon, the Fermi level is near the valence band edge, so most mid-gap traps will capture holes and reduce the majority carrier concentration. The change in hole concentration in p-type silicon as a function of proton fluence can be expressed by:

$$\Delta p = p_\phi - p_0 = -\sum I_{tj} f(E_{ij})\phi \approx -R_c\phi$$

where p_ϕ is the carrier concentration after irradiation, I_{tj} is introduction rate of the *j*th majority carrier center by radiation, $f(E_{ij})$ is the capture rate of majority carriers by the *j*th majority carrier trap center, ϕ is the proton fluence, and R_c is the carrier removal rate, which depends on the proton energy. The absolute values for R_c in p-type silicon are approximately expressed by:

$$R_c = 573 E_p(MeV)^{-1.138} cm^{-1}$$

where E_p is the proton energy.

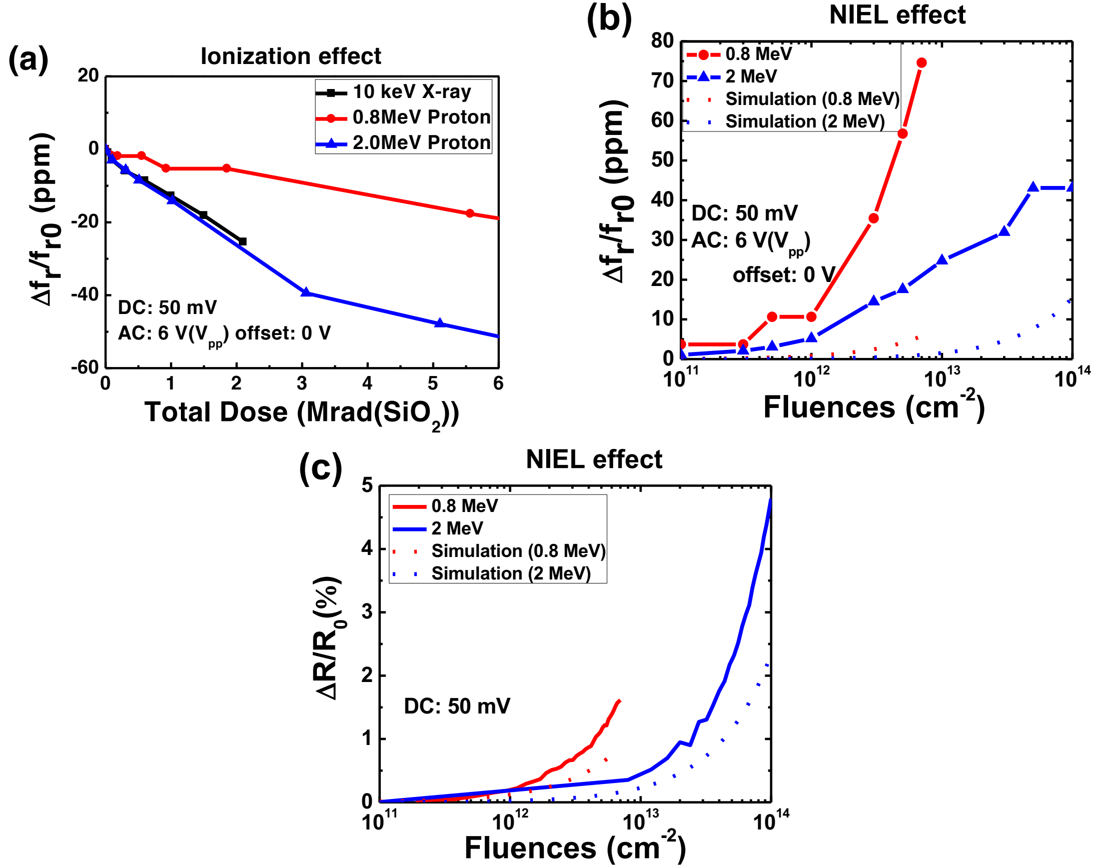

Figure 11. (a) Ionization-induced resonant frequency changes for proton irradiation and X-ray irradiation; (b) NIEL induced resonant frequency changes for proton irradiation. Solid lines: extracted NIEL induced change; dashed lines: simulation results based on carrier removal effects; (c) anchor resistance change during proton irradiation. Solid lines: experimental results; dashed lines: simulation results based on carrier removal.

The change in carrier concentration affects the elastic modulus, which will affect the resonance frequency of MEMS resonators. Keyes demonstrated in 1961 that dopant atoms cause a decrease in the shear elastic modulus c44 in semiconductors. A change in elastic modulus due to a change in carrier concentration has also been observed above. The resonant frequency change can be calculated from the change in carrier concentration:

$$\Delta c_{44} = -\frac{1}{5}\left(\frac{8\pi}{3}\right)^{\frac{2}{3}}\frac{d^2}{h^2}\left(m_{v1}{}^{*}p_1^{\frac{1}{3}} + m_{v2}{}^{*}p_2^{\frac{1}{3}}\right)$$

$$Y_{110} = \frac{4(c_{11}-c_{12})(c_{11}+2c_{12})c_{44}}{2c_{11}c_{44}+(c_{11}-c_{12})(c_{11}+2c_{12})}$$

$$\Delta f_r / f_{r0} \propto \Delta Y / Y_0$$

where Δc_{44} is the change in modulus with respect to the value of intrinsic silicon, *d* is the deformation potential (15.4 eV), *h* is Planck's constant, $m_{v1}{}^{*}$ is the light hole effective mass, $m_{v2}{}^{*}$ is the heavy hole effective mass, p_1 is the concentration of light holes, p_2 is concentration of heavy holes, and Y_{110} is the Young's modulus along the [110] direction, which most strongly affects the resonant frequency.

The dashed lines in Figs. 11b and 11c are calculation results based on carrier removal, which show similar trends with the experimental results. The calculation results underestimate the real change for both resonant frequency and anchor resistance. This is caused by the underestimation of the carrier removal rate R_c , which is based on empirical results obtained from p-type silicon with a resistivity of about 10 Ω-cm (~10^{15} cm^{-3}). The MEMS resonators in this work are fabricated from heavily doped p-type silicon with a resistivity of 0.036 Ω-cm (~10^{18} cm^{-3}). The Fermi level for the heavily doped material is much closer to the valence band edge than the p-type silicon in, which results in more holes captured by mid-gap traps. Eventually, this produces larger degradation in both resonant frequency and anchor resistance.

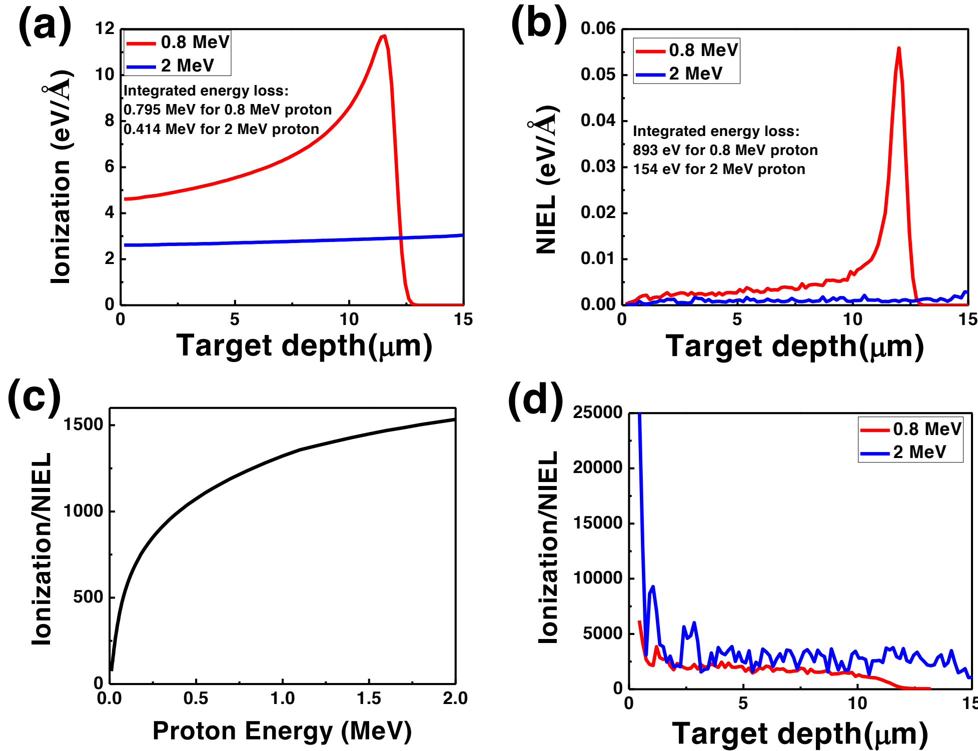

Figure 12. SRIM simulation results for protons in silicon: (a) ionization and (b) NIEL in silicon due to 0.8 MeV protons and 2 MeV protons; (c) ionization vs NIEL in silicon for protons with various energies; (d) ionization vs NIEL in silicon for 0.8 MeV protons and 2 MeV protons.

Stopping power and Range of Ions in Matter (SRIM) simulation results of protons in silicon are shown in Fig. 12. For both 2 MeV and 0.8 MeV protons, much more energy goes into ionization than NIEL, as shown in Figs. 12a and 12b. The energy loss distribution is quite different. For 2.0 MeV proton irradiation, energy loss is distributed nearly uniformly inside the silicon, causing a uniform carrier concentration change. For 0.8 MeV protons, the energy loss peaks inside the silicon, consistent with the projected range of 11.74 μm. The generated defect density will be much larger at this location than in the rest of the device. This non-uniform defect distribution produces an internal strain gradient inside the silicon and affects the elastic properties.

The ratio of energy lost to ionization to that lost to NIEL decreases as proton energy decreases, as shown in Fig. 12c. This suggests that NIEL effects are more important for low energy proton irradiation. Fig. 12d shows changes in energy lost to ionization and NIEL as protons transport through 15 μm of silicon, which

is the thickness of the MEMS resonator. Ionization contributes relatively larger effects for 2 MeV protons than for 0.8 MeV protons, which is consistent with the experimental results presented above.

IV) Dose-Rate Effects on the Total-Ionizing-Dose Response of Piezoresistive Micromachined Cantilevers

In this part of the work, the dose-rate dependence of the total-ionizing-dose (TID) response is evaluated for T-shaped asymmetric piezoresistive micromachined cantilevers. The work described above shows sensitivity to X-ray and ultraviolet radiation but does not evaluate dose-rate dependence. Understanding dose-rate effects in MEMS is crucial, as these types of devices are considered for space applications where ionizing dose rates are much lower than those typically used for ground testing.

Negative resonance frequency shifts are induced by 10-keV X-rays and are found to depend significantly on the dose-rate, with greater negative shifts at lower dose rates. Further tests with hydrogenated devices show no measurable differences between hydrogenated and untreated devices for nominal operation, but larger shifts were observed at low dose rate for hydrogenated devices in radiation testing. These differences in response are attributed to differences in rates of surface charging at high and low dose rates, as well as to the complex interplay among transport and reactions of hydrogen in silicon, leading to dopant deactivation and/or passivation. Each of these effects is a potential source of increased carrier densities in the cantilevers. These mechanisms are more significant at low dose rates than at higher dose rates because higher densities of hydrogen in Si favor bimolecular recombination reactions over the transport and reactions with dopants that lead to the enhanced low-dose-rate response, and space charge effects are more significant at high dose rates than low dose rates. Excess carriers affect Young's modulus and therefore the resonance frequency.

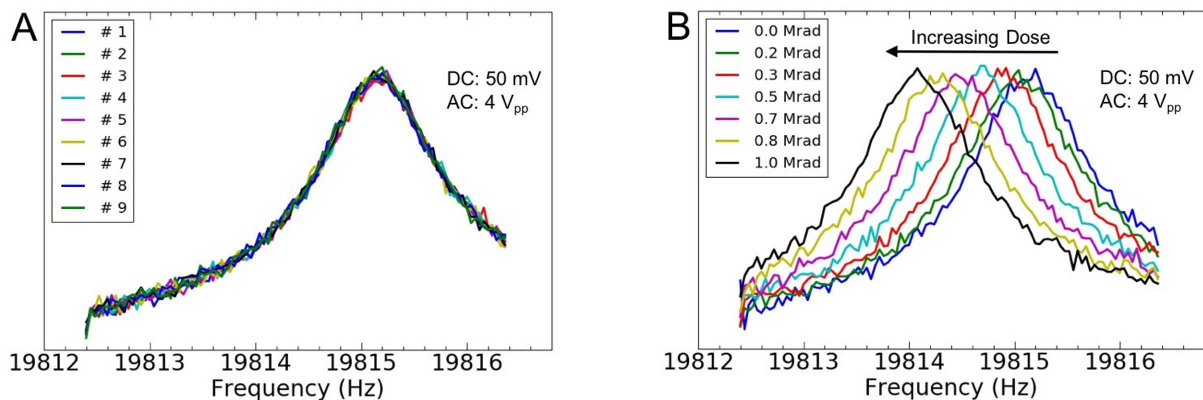

Figure 13. Frequency response of the cantilever near the resonance peak (a) for 9 repeated sweeps before irradiation, showing the device stability, and (b) as a function of increasing dose.

The fabrication and measurement of the cantilevers is the same as described above. All cantilevers were irradiated using a 10-keV X-ray source in a vacuum chamber with a 25.4-μm thick beryllium window that reduces X-ray intensity by ~0.3%. Devices were operating dynamically before, during, and after irradiation. Each device was swept over a 2 Hz range containing its resonance peak. Experiments were performed at a temperature of ~295 K and pressure of ~1x10^{-4} mbar. Each cantilever was in vacuum for a minimum of 12 h before irradiation to allow the cantilevers to outgas and ensure pressure stability. Control devices

were irradiated to doses from 200 krad(SiO_2) to 1 Mrad(SiO_2) at rates from 5.4 to 30.3 krad(SiO_2)/min, and devices subjected to a steam bath for an hour immediately before irradiation were irradiated to 1 Mrad(SiO_2) at rates from 5.4 to 30 krad(SiO_2)/min. Fig. 13 shows (a) the stability of the resonance frequency before irradiation, and (b) a sample of the resonance peak frequency shifting lower during a 5.4 krad(SiO_2)/min test. At least two devices were irradiated under each set of irradiation conditions. Devices were monitored for post-irradiation behavior at room temperature for 20 h or until the resonance frequency had recovered or exceeded its pre-irradiation value.

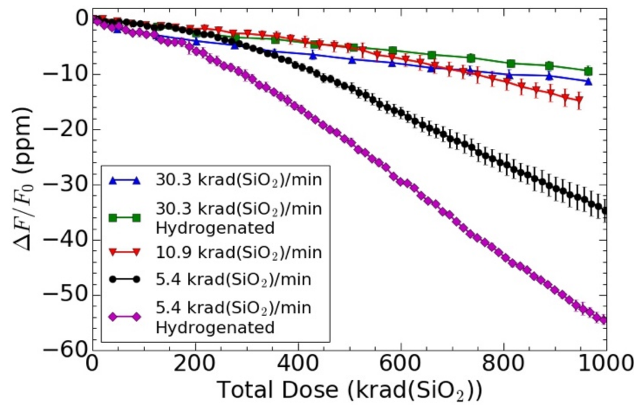

Figure 14. Resonance peak as a function of total dose for devices irradiated at 5.4, 10.9, and 30.3 krad(SiO2)/min, and for hydrogenated devices irradiated at 5.4 and 30.3 krad(SiO2)/min. Error bars are standard deviations.

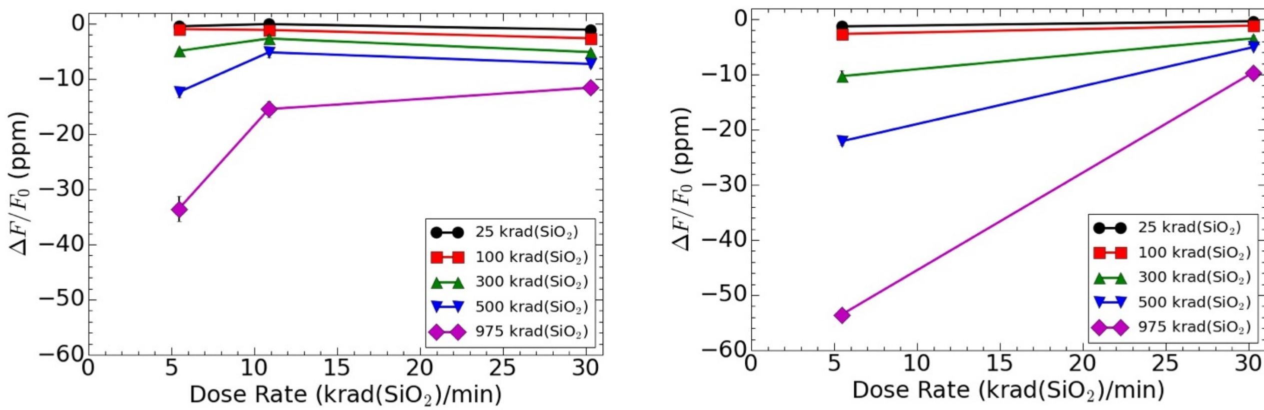

Figure 15. Resonance peak as a function of dose rate (a) for devices irradiated at 5.4, 10.9, and 30.3 krad(SiO2)/min, and (b) for hydrogenated devices irradiated at 5.4 and 30.3 krad(SiO2)/min. Error bars are standard deviations.

Each resonance sweep is fit with a combination of linear and Lorentzian function to determine the resonance frequency of each sweep. Fig. 14 shows the fractional change in resonance frequency as a function of dose for devices irradiated at 30.3, 10.9, and 5.4 krad(SiO2)/min, and for hydrogenated devices irradiated at 30.3 and 5.4 krad(SiO2)/min. The error bars shown are standard deviations. Both normal and hydrogenated devices irradiated at 30.3 krad(SiO2)/min show shifts of ~ -10 ppm after 1 Mrad(SiO2). Devices irradiated at 10.9 krad(SiO2) show frequency

shifts of ~ -15 ppm after 1 Mrad(SiO_2). Hydrogenated devices irradiated at 5.4 krad(SiO_2)/min show a similar shape but a 57% increase in magnitude of shift compared to the non-hydrogenated counterparts. Figure 15 shows the shifts in resonance frequency as a function of dose rate for both non-hydrogenated (a) and hydrogenated devices (b).

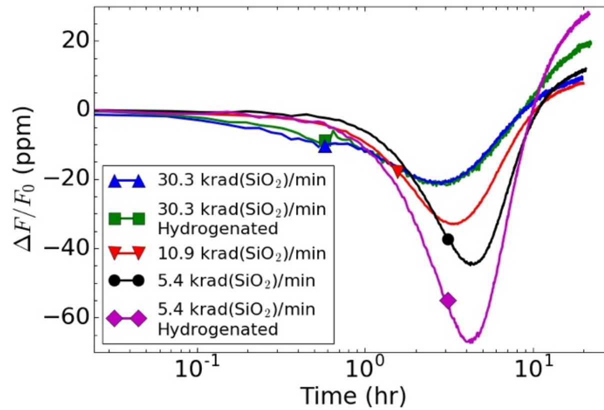

Figure 16. Resonance peak as a function of time during and after irradiation for representative devices irradiated at 5.4, 10.9, and 30.3 krad(SiO2)/min and hydrogenated devices irradiated at 5.4 and 30.3 krad(SiO2)/min, and subsequent annealing. The marker on each data set indicated the time at which irradiation ended and annealing began.

Figure 16 shows the change in resonance frequency as a function of time with a marker denoting where irradiation ends and annealing begins. Each of the devices recovers to or beyond its pre-irradiation resonance frequency value approximately 10 hours after the beginning of irradiation. The resonance frequency of some devices continues to increase post-irradiation most likely due to the slow decrease in pressure of the vacuum and resulting outgassing from the cantilever over 40 h. Also observed are the shifts in resonance frequency as a function of dose rate for non-hydrogenated and hydrogenated devices. The resonance frequency decreases more with TID for devices irradiated at the lowest rate, with the largest changes occurring for hydrogenated devices irradiated at low dose rates. Regardless of dose rate or hydrogen content, devices all recover to similar values after irradiation, independent of test condition.

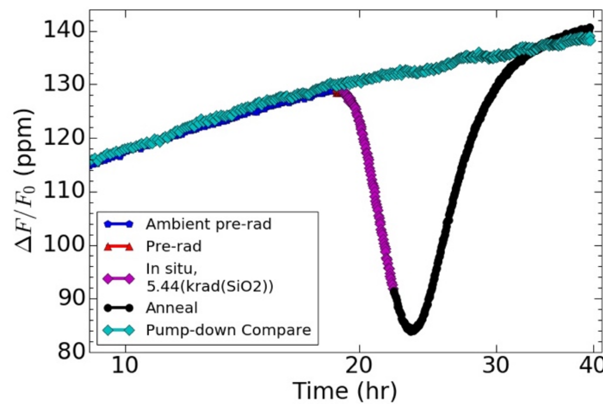

Figure 17. Resonance peak as a function of time for devices that were either unirradiated or irradiated at 5.4 krad(SiO2)/min, showing that the primary effect of irradiation is to decrease the resonance frequency significantly from the level to which it otherwise would have increased as a result of the continuing pump-down process.

Fig. 17 compares the evolution of the resonance frequency with time for unirradiated and irradiated devices that were not exposed to hydrogen over the same time periods. This emphasizes that the primary effect of irradiation is to decrease the resonance frequency significantly from the level to which it otherwise would have increased as a result of the continuing pump-down process. The degree to which the resonance frequency decreases from this level is influenced strongly by the dose and dose rate of the irradiation, as well as (for lower-rate irradiation, whether the device has been hydrogenated. Hence, the differences observed in Figs. 14-16 are due to true dose-rate effects and not time-dependent effects.

Resonance frequency shifts due to irradiation are related to how Young's modulus depends on carrier concentration, how hydrogen in silicon interacts with silicon, boron, and other hydrogen atoms [11], and time-dependent surface charging of the native oxide. We now consider how the interplay of these factors may lead to the effects observed in Figs. 13-17.

For an isotropic, homogenous material, the relationship between stress (σ) and strain (ε) is defined by Hooke's Law,

$$\sigma = C\varepsilon \quad (2)$$

where C can be represented by a constant value of Young's modulus (Y). In single crystal silicon, elasticity is orientation dependent, necessitating the use of tensors to fully describe the direction of applied stress and force. This requires a fourth-rank tensor to describe the stiffness by relating the second-rank tensors of stress and strain. Silicon's cubic symmetry, however, allows this to be condensed to a 6 × 6 matrix with only three independent components. The cantilevers used in these experiments have force applied in the [110] direction, allowing Young's modulus to be simplified to:

$$Y_{110} = \frac{4(c_{11}+c_{12})(c_{11}-c_{12})c_{44}}{2c_{11}c_{44}+(c_{11}+2c_{12})(c_{11}-c_{12})}$$

where c_{11}, c_{12}, and c_{44} are stiffness constants.

Young's modulus is affected by carrier concentration with the effect originating from a change in the Fermi level due to strain removing band degeneracy. In general, free carrier concentrations relating to the elastic constant are used to calculate the free energy of the crystal with and without strain. For *p*-type materials, the energies and momenta for holes can be calculated where a portion of the energy comes from strain, as shown by Csavinszky and Einspruch. Keyes has shown that only the shear elastic constant, c_{44}, is affected by the presence of dopant atoms. From this, the change in shear elastic constant from holes can be calculated:

$$\Delta c_{44} = -\frac{1}{5}\left(\frac{8\pi}{3}\right)^{2/3}\left(\frac{m_p{}^{*}\Xi^2 p^{1/3}}{h^2}\right)$$

where c_{44} is the elastic constant, $m_p{}^{*}$ is the hole effective mass, Ξ is the shear deformation potential, *p* is the hole concentration, and *h* is Planck's constant.

Atomic hydrogen is introduced into silicon throughout the wafer and device fabrication processes and has complex behavior that depends on the doping, including passivation of shallow impurities. In *p*-type

material, boron is passivated by direct compensation of the electron from H annihilating a free hole and forming H^+ . The hydrogen also causes relaxation of the Si crystal, adding new energy levels. Ionizing radiation creates electron-hole pairs in Si and the native oxide. The transporting carriers can lead to surface charging of the native oxide as well as the release of hydrogen in the Si and native oxide. Once H^+ has been formed, it has high mobility in Si because its energy barrier for transport in ~ 0.2 eV. Transporting hydrogen in the Si can react with a hydrogen-passivated B dopant, activating the dopant and forming H_2, which diffuses out of the system. Transporting hydrogen can also passivate activated dopant atoms.

Whether the passivation or activation reaction dominates the response depends on the relative densities of activated and hydrogen-passivated dopant atoms, the concentration of hydrogen, temperature, bias, etc. Surface charging effects will influence the local electric fields and carrier densities as well. Hence, it is difficult to quantify the relative effects of surface charge and hydrogen on the changes in resonance frequency. However, because similar factors are at play in linear bipolar transistors that exhibit enhanced low-dose-rate sensitivity (ELDRS) it is perhaps not surprising that somewhat similar dose rate effects are observed in these devices under these irradiation and measurement conditions, as we now discuss.

When the transporting hydrogen concentration is relatively higher, as is the case for the higher-rate irradiations in Figs. 14-16, transporting hydrogen atoms in the Si and/or SiO_2 can dimerize to form H_2 with higher probability than when the transporting hydrogen concentration is lower, as is the case for lower-rate irradiations. The resulting loss of hydrogen in atomic form reduces the amount available to potentially depassivate dopant atoms at higher dose rates than at lower dose rates. At higher rates, soaking the devices in hydrogen is therefore ineffective in changing resonance frequency shifts in Fig. 16 because the extra hydrogen simply recombines through this process and leaves the system without reaction with B dopants. At lower dose rates, on the other hand, extra hydrogen is available to react with B, leading to higher carrier concentrations and larger resonance frequency shifts.

The above process is analogous to the sequence of events involving similar hydrogen transport and reactions in SiO_2 that can lead to ELDRS in linear bipolar transistors. Adding to the effects of the newly activated dopant atoms on the decrease in resonance frequency is the buildup of surface charges on the native oxide, which is also potentially dose-rate sensitive due to space charge effects that can enhance the neutralization of trapped charge at higher dose rates. This may not only reduce the surface-charge density, but also reduce the number of transporting holes that would otherwise be available to liberate H^+, which is a key element that determines whether oxides exhibit ELDRS.

The ongoing transport of hydrogen within the Si and/or from the native oxide into the Si may also explain the continuing decline in frequency immediately after irradiation, before the resonance frequency recovers to its initial value, as shown in Fig. 16. During the first phase of this process the depassivation of B-H complexes in the system evidently dominates the response, increasing the carrier density further.

Figs. 16 and 17 show the responses of all devices recovering to equilibrium values of resonance frequency that the devices would otherwise have shown in the absence of irradiation. This indicates that the surface charge has been neutralized, and that passivation reactions have restored the concentrations of active B dopants and passivated B-H complexes to values closer to ones observed before irradiation. The variations in post-irradiation values in Fig. 16 suggest that this return to near-equilibrium is only approximate, which is not surprising, since the final densities of H and B-H likely differs from initial values.

While the above discussion is qualitative in nature, we emphasize that these devices clearly show true dose rates, and a strong sensitivity to hydrogen treatments for lower-rate irradiation. Future work will be

required to quantify these effects in ways similar to those developed for ELDRS after many years of research. Until such understanding is developed, detailed testing of these types of MEMS devices will need to consider dose rate and hydrogen effects in device characterization and qualification.

V) Near-Surface Electronic Contribution to Semiconductor Elasticity

Finally, we explore how ultraviolet (UV) radiation influences the elastic properties of a micro scale silicon resonator. UV radiation differs from X-ray radiation in that the penetration depth is much lower (<15 nm), so that any observed changes should be due to the impact of the UV radiation on the near surface region. UV induced changes in the carrier concentration are detected using four-terminal resistance measurements. Simultaneously monitoring the resonant frequency of the resonator shows that the Young's modulus decreases as the carrier concentration increases, clearly demonstrating the impact of the free carrier concentration on the elasticity, independent of dopant concentration. Theoretical modeling shows that the impact of the surface carrier concentration on the elasticity increases dramatically as the surface to volume ratio of the resonator increases, implying that nanoscale electromechanical systems will be highly susceptible to near surface carrier concentration induced changes to the Young's modulus.

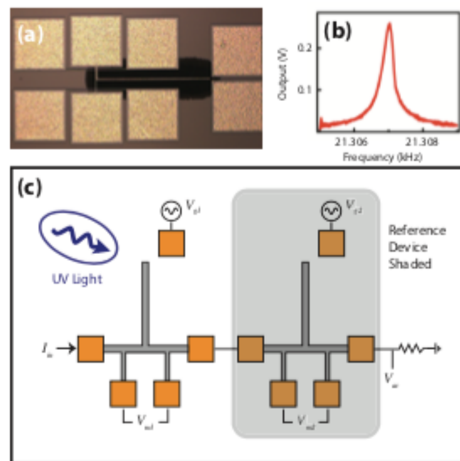

Figure 18. (a) Optical microscope image of the resonator. The resonator beam is 655 microns long, 8 microns wide, and 15 microns thick. The voltage contacts on the base are separated by 110 microns. (b) Output versus driving frequency for a representative device. Nine different scans are plotted together to demonstrate the device reproducibility. (c) Schematic showing the measurement configuration. The asymmetric base is not shown.

Figure 18 shows the device layout and experimental set-up. The starting material for the resonator is a silicon-on-insulator (SOI) wafer with a device layer thickness of 15 microns, a buried oxide layer thickness of 2 microns and a handle layer thickness of 500 microns. The device layer is boron doped (p-type) to a resistivity of approximately 0.013 ohm-cm. T-shaped cantilevers are defined in the device layer using DRIE, and then released from the backside by subsequent dry etching. Prior to measurement, the sample chamber is evacuated using a turbo-molecular pump. The chamber is pumped for 72 hours, until the pressure is constant as measured at the pump inlet. The cantilever beam is actuated by an AC voltage on a nearby gate electrode and is continuously driven during the course of the measurement.

The resistance of the base changes with the strain of the moving cantilever due to the piezoresistivity of the silicon, so that cantilever motion can be detected by monitoring the ac voltage generated across a sense resistor in series with the base. The base has an asymmetric design to maximize the resistance change. Figure 18(b) shows the frequency response of a representative device measured in a vacuum chamber at a pressure of 2×10^{-6} mbar. A peak is observed at frequency of 21.307 kHz; high speed camera imaging confirms that this peak correlates with the cantilever resonance. In subsequent measurements, the resonant frequency of the cantilever and the four-terminal resistance of the base are monitored while the sample is exposed to light through a quartz window in the vacuum chamber. For reference, a second resonator is placed adjacent to the test device but shielded from the light by a metal plate (see Fig. 18(c)). Comparison between the exposed and unexposed samples allows for changes due to carrier generation to be isolated from those due to temperature.

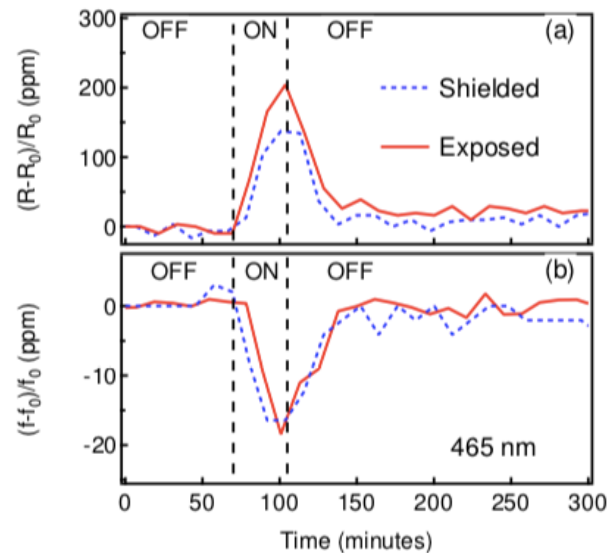

Figure 19. (a) Change in in the four-terminal resistance of the resonator beam and (b) change in the resonant frequency, for samples exposed and shielded from 465 nm blue light.

As an initial demonstration of the measurement technique, the resonator was exposed to blue light of energy below the oxide band edge. The blue light source is an Engin LZ1-10D800 LED with peak wavelength of 425 nm and measured output power of 1.44 mW. Figure 19 shows the (a) four terminal resistance and (b) resonant frequency plotted as a function of time before, during, and after a 30 minute exposure to light from the 465 nm LED. The resistance increases and the resonant frequency decreases during exposure, with a similar change being observed in both shielded and unshielded devices. It is known that the silicon hole mobility and Young's modulus both decrease with increasing temperature, so that the observed changes can be attributed to heating of the sample chamber. Once the light is removed, the original signal is recovered in approximately 20 minutes, providing a measure of the thermal recovery time for the resonator. By comparison, Fig. 20 shows the impact that UV light from a 255 nm LED has on (a) the four-terminal resistance and (b) the resonance frequency. The UV source is a Thorlabs LED255J Optan UV LED with measured output power of 220 µW. The shielded device is now used to monitor the heating caused by the UV light; its resistance increases and resonant frequency decreases as before, and both recover in approximately 20 minutes following exposure. The exposed sample behaves very differently. Its resistance drops a large amount (rather than rising), while the resonant frequency drops below the reference value of the shielded device. Neither recover back to their original values over the 300 minute measurement.

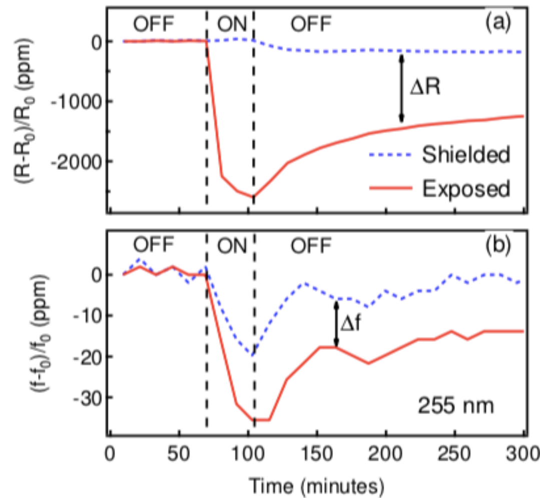

Figure 20. (a) Change in in the four-terminal resistance of the resonator beam and (b) change in the resonant frequency, for samples exposed and shielded from 255 nm UV light.

The difference in signal between the shielded and exposed devices gives the change due to the UV light that is not due to heating. This is plotted as a function of time in Fig. 21 for the (a) resistance ΔR and for the (b) resonance frequency Δf. Both drop sharply following UV exposure, and then slowly recover back to their original values over approximately 60 hours. The similarity between the resistance recovery and the resonance frequency recovery suggests that the two are related, even though the total resistance change (2500 ppm) is 100 times larger than the total frequency change (25 ppm). Further analysis shows that the resistance and resonant frequency recover to their equilibrium values logarithmically with time, as is observed for many slow relaxation processes. Measurements were repeated for 5 different sets of samples, and in each case, similar results were observed.

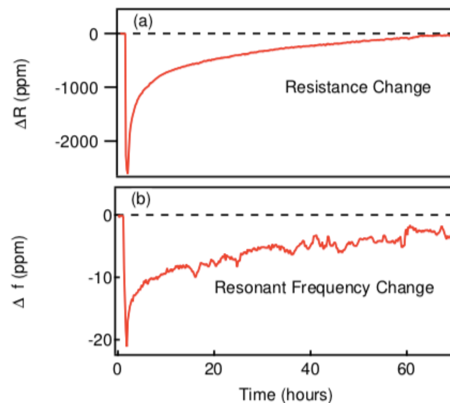

Figure 21. Difference between (a) the four-terminal resistance ΔR and (b) the resonant frequency Δf for the exposed sample and reference sample measured as a function of time following a 30 minute exposure to 255 nm light.

The effect of UV light on a silicon surface is well known. UV light is absorbed in the near surface region (with an absorption depth of 10 nm for 255 nm light). This creates highly excited electron-hole pairs with energies above the conduction and valence bands of the overlying native silicon oxide layer. Some amount of the excited charge Qox is transferred to the oxide, where it becomes trapped. Photovoltage and second

harmonic generation experiments have shown that the trapped oxide charge has an extremely long lifetime, and slowly decays over a period of 2-3 days following UV exposure. The surface oxide charge is balanced by an equal but opposite charge due to the accumulation or depletion of carriers in the underlying silicon. In the following it is shown that this change in surface carrier concentration can account for our experimentally observed behavior: the resistance of the silicon drops due to carrier concentration dependence of the conductivity, and the resonance frequency drops due to the carrier concentration dependence of the Young's modulus.

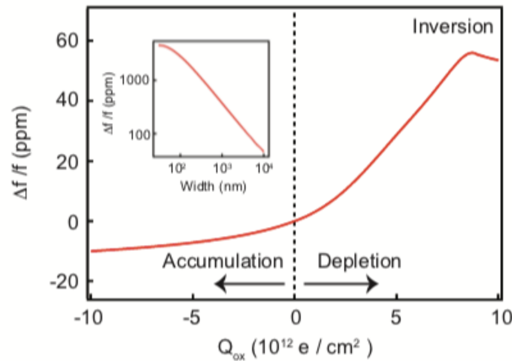

Figure 22. Relative change in resonant frequency as a function of oxide charge calculated using model calculations. The inset shows the relative change in resonant frequency as a function of beam width plotted on a log-log scale. The oxide charge is taken to be $Q_{ox} = 8.71 \times 10^{13}$ e/cm^2.

The impact of the surface oxide charge on the resonant frequency, while clearly detected, is relatively small for this microscale cantilever beam. As the device dimensions decrease and the surface-to-volume ratio increases, the impact of surface charging will also increase. The inset to Fig. 22 shows the maximum calculated change in resonant frequency due to an increase in surface oxide charge of 8.7 x10^{12} cm^{-2} as function of cantilever beam width. The resonant frequency change increases rapidly with decreasing dimensions and is greater than 3000 ppm for sub 100 nm width beams. This is a substantial amount for MEMS oscillator applications where 1-10 ppm stability is desirable in order to substitute for quartz crystals in commercial applications. The effects we describe were demonstrated for UV light, however, they would also occur for any type of radiation (gamma rays, high energy protons) with energy above the silicon / silicon-dioxide energy barrier. UV radiation can be easily blocked with a lightweight shield but blocking space radiation requires a large amount of mass, negating the advantages of light-weight MEMS technology. The change in resonant frequency eventually saturates with constant UV exposure, however, exposure to high energy radiation would generate more surface states, making the resonator progressively more susceptible to radiation damage. Radiation induced changes in mechanical properties due to carrier concentration changes would be particularly important in materials that exhibit persistent photoconductivity. This includes many compound semiconductors (including GaN and ZnO) amorphous silicon, and semiconductor nanostructures and membranes. It is also noted that the instabilities and electric field induced shifts reported in the literature for nanometer scale resonators could in part be attributable to surface carrier concentration changes.

VI) Conclusion

MEMS resonator studies revealed fundamental mechanisms by which radiation influences MEMS devices The carrier concentration is modified by radiation due to dopant de-passivation and surface charging and this changes the elastic constants. The effects become substantial as the device dimensions reduced. The resulting sensitivities of the resonance frequency shifts to the radiation dose rate and to hydrogen are therefore important factors to consider in device characterization and qualification testing for use of these devices in space radiation environments.

REFERENCES (Published Journal Articles)

1. Shuvra, Pranoy Deb; McNamara, Shamus; Lin, Ji-Tzuoh; Alphenaar, Bruce; Walsh, Kevin; Davidson, Jim; 'Axial asymmetry for improved sensitivity in MEMS piezoresistors,' *Journal of Micromechanics and Microengineering*,**26**,9,095014,2016
2. Gong, Huiqi; Liao, Wenjun; Zhang, En Xia; Sternberg, Andrew L; McCurdy, Michael W; Davidson, Jim L; Reed, Robert A; Fleetwood, Daniel M; Schrimpf, Ronald D; Shuvra, Pranoy Deb; ,'Total-ionizing-dose effects in piezoresistive micromachined cantilevers,' *IEEE Transactions on Nuclear Science*, **64**, 1, 263-268, 2016
3. Arutt, Charles N; Alles, Michael L; Liao, Wenjun; Gong, Huiqi; Davidson, Jim L; Schrimpf, Ronald D; Reed, Robert A; Weller, Robert A; Bolotin, Kirill; Nicholl, Ryan; ,'The study of radiation effects in emerging micro and nano electro mechanical systems (M and NEMs),' *Semiconductor Science and Technology*, **32**, 1, 013005, 2016
4. Lin, Ji-Tzuoh; Shuvra, Pranoy D; Liao, Wenjun; McNamara, Shawns; Walsh, Kevin M; Arutt, Charlie N; Gong, Huiqi; Davison, Jim L; Alles, Michael L; Alphenaar, Bruce W; ,'Surface carrier concentration effect on elastic modulus of piezoelectric MEMS silicon cantilevers,' *2017 19th International Conference on Solid-State Sensors, Actuators and Microsystems (TRANSDUCERS),* 1175-1178, 2017
5. Gong, Huiqi; Liao, Wenjun; Zhang, En Xia; Sternberg, Andrew L; McCurdy, Michael W; Davidson, Jim L; Reed, Robert A; Fleetwood, Daniel M; Schrimpf, Ronald D; Shuvra, Pranoy Deb; 'Proton-induced displacement damage and total-ionizing-dose effects on silicon-based MEMS resonators,' *IEEE Transactions on Nuclear Science*, **65**, 1, 34-38, 2017
6. Lin, JT; Shuvra, PD; McNamara, S; Gong, H; Liao, W; Davidson, JL; Walsh, KM; Alles, ML; Alphenaar, BW; 'Near-surface electronic contribution to semiconductor elasticity,' *Physical Review Applied*, **8**, 3, 034013, 2017
7. Arutt, Charles N; Liao, Wenjun; Gong, Huiqi; Shuvra, Pranoy Deb; Lin, Ji-Tzuoh; Alles, Michael L; Alphenaar, Bruce W; Davidson, Jim L; Walsh, Kevin M; McNamara, Shamus; 'Dose-rate effects on the total-ionizing-dose response of piezoresistive micromachined cantilevers,' *IEEE Transactions on Nuclear Science*, **65**, 1, 58-63, 2017
8. Arutt, Charles N; Shuvra, Pranoy Deb; Lin, Ji-Tzuoh; Alles, Michael L; Alphenaar, Bruce W; Davidson, Jim L; Walsh, Kevin M; Mcnamara, Shamus; Fleetwood, Daniel M; Schrimpf, Ronald D; 'Dopant-Type and Concentration Dependence of Total-Ionizing-Dose Response in Piezoresistive Micromachined Cantilevers,' *IEEE Transactions on Nuclear Science*, **66**, 1, 397-404, 2018

9. Shuvra, Pranoy Deb; Arutt, Charles N; Lin, Ji-Tzuoh; Davidson, Jim; Alles, Michael; Walsh, Kevin; Alphenaar, Bruce; McNamara, Shamus; 'Dimensional dependence of the radiation damage in microelectromechanical system resonators,' *Journal of Physics D: Applied Physics*, **52**, 37, 375101,2019
10. Chen, Hailong; Jia, Hao; Shuvra, Pranoy Deb; Lin, Ji-Tzuoh; Alphenaar, Bruce W; Feng, Philip X-L; 'GaN/AlN heterostrucutre micromechanical self-sustained oscillator for middle ultraviolet (MUV) light detection,' *2019 IEEE 32nd International Conference on Micro Electro Mechanical Systems (MEMS),* 644-647, 2019
11. Lin, Ji-Tzuoh; Wang, Peng; Shuvra, Pranoy; McNamara, Shamus; McCurdy, Mike; Davidson, Jim; Walsh, Kevin; Alles, Mike; Alphenaar, Bruce; 'Impact of X-Ray Radiation on GaN/AlN MEMS Structure and GaN HEMT Gauge Factor Response,' *2020 IEEE 33rd International Conference on Micro Electro Mechanical Systems (MEMS)*, 968-971,2020
12. Lin, Ji-Tzuoh; Shuvra, Pranoy Deb; Yang, Jerry A; McNamara, Shamus; Walsh, Kevin; Alphenaar, Bruce; 'Buckled beam mechanical memory using an asymmetric piezoresistor for readout,' *Journal of Micromechanics and Microengineering*, **30**, 7, 075006, 2020.